IOP Publishing
Journal of Physics D: Applied Physics
J. Phys. D: Appl. Phys. 56 (2023) 505301 (10pp)
https://doi.org/10.1088/1361-6463/acf86b

Detailed pathway for a fast low-temperature synthesis of strongly thermochromic W-doped VO_2 films with a low transition temperature

Jaroslav Vlček*, Michal Kaufman, Andrea Dagmar Pajdarová, Stanislav Haviar, Radomír Čerstvý, Jiří Houška and Mina Farahani

Department of Physics and NTIS–European Centre of Excellence, University of West Bohemia, Univerzitní 8, 30614 Plzeň, Czech Republic

E-mail: vlcek@kfy.zcu.cz

Received 22 May 2023, revised 4 September 2023
Accepted for publication 11 September 2023
Published 21 September 2023

Abstract

We report the discharge characteristics, and population of chosen atomic neutral (V, O and Ar) and ionic (V^+, V^{2+}, O^+ and Ar^+) species in the discharge during low-temperature (350 °C) depositions of W-doped VO_x films onto a 170 nm thick Y-stabilized ZrO_2 layer on a 1 mm thick conventional soda-lime glass. The depositions were performed using reactive deep oscillation magnetron sputtering with a pulsed O_2 flow control and to-substrate O_2 injection into a high-density plasma in front of the sputter V-W target. The pre-selected critical values of the oxygen partial pressure were in the range from 82 mPa to 92 mPa. Optical emission spectroscopy proved a relatively high density of O atoms in front of the substrate, which is important for production of the W-doped VO_2 films. It was found that setting of the amount of O_2 in the gas mixture determines not only the elemental and phase composition of the films and their deposition rate but also the crystallinity of the thermochromic VO_2 phase in them. The crystalline W-doped VO_2 films with a low transition temperature of 28 °C exhibited a high modulation of the solar energy transmittance of 8.9%. The results are important for further improvement of this new scalable sputter deposition technique for a fast (53 nm min^{-1} at a target-substrate distance of 100 mm in this work) low-temperature synthesis of high-performance durable thermochromic VO_2-based multilayer coatings designed for smart-window applications.

Keywords: thermochromic W-doped VO_2, high-power impulse magnetron sputtering, pulsed O_2 flow control, sensitivity to oxygen partial pressure, atomic and ionic species

(Some figures may appear in colour only in the online journal)

1. Introduction

Vanadium dioxide (VO_2) is a thermochromic material that exhibits a reversible phase transition from a low-temperature monoclinic VO_2 (M1) semiconducting phase to a high-temperature tetragonal VO_2 (R) metallic phase at a transition temperature, T_{tr}, of approximately 68 °C (bulk VO_2 [1]). This phase transformation is accompanied by a strong decrease in the infrared transmittance, and by a strong increase in electrical and thermal conductivity, which make VO_2-based films a promising candidate for numerous applications, such

* Author to whom any correspondence should be addressed.

© 2023 IOP Publishing Ltd

as electronic and optical switches, thermal sensors, smart radiator devices, adaptive thermal camouflage and energy-saving smart windows with automatically varied solar energy transmittance (see, for example [2–8], and the works cited therein).

Magnetron sputter deposition with its versatility and the ease of scaling up to large substrate sizes is probably the most important preparation technique of thermochromic VO_2-based coatings, particularly for future smart-window applications [8–12]. Note that magnetron sputter sources are used very frequently not only in glass production lines (e.g. for deposition of low-emissivity coatings) but also in large-scale roll-to-roll deposition devices [13, 14] producing coatings on ultrathin (0.02–0.20 mm) flexible glass or polymer foils. Here, it should be mentioned that the application potential of the thermochromic VO_2-based coatings depends on the ability to achieve not only the VO_2 stoichiometry but also the crystallization of the thermochromic VO_2 phase under as industry-friendly process conditions as possible, i.e. at a maximum substrate surface temperature, T_s, during the preparation (deposition and possible post-annealing) close to 300 °C [8–10, 15, 16] and without any substrate bias voltage [17]. Moreover, desirable and challenging lowering of T_{tr} toward room temperature using doping of VO_2 by other elements (such as W) should be performed without any degradation of thermochromic properties of doped VO_2 films [6, 8, 18, 19].

Reactive high-power impulse magnetron sputtering (HiPIMS) is a promising scalable deposition technique for a low-temperature (300 °C–350 °C) preparation of thermochromic VO_2-based films [14]. HiPIMS is characterized by highly ionized fluxes of particles with high fractions of ionized sputtered metal atoms onto the substrate and by enhanced energies and momenta of the ions bombarding the growing films, allowing one to achieve film densification and crystallinity at a low substrate temperature and without a substrate bias voltage (see, for example [17]). Recently, low-temperature HiPIMS depositions of thermochromic undoped VO_2 films [15, 16, 20–22] and strongly thermochromic ZrO_2/W-doped VO_2/ZrO_2 coatings [23] have been reported.

In our recent paper [24], we presented a scalable sputter deposition technique for the preparation of strongly thermochromic YSZ/W-doped VO_2/YSZ coatings, where YSZ denotes the Y-stabilized ZrO_2, on conventional soda-lime glass (SLG) at $T_s = 350$ °C and without any substrate bias voltage. The thermochromic W-doped VO_2 layers were deposited using a controlled deep oscillation magnetron sputtering (DOMS) of a single V-W target. The DOMS is a modified version of HiPIMS with packages (macropulses) of short high-power micropulses [25, 26]. Our motivation to apply this high-power discharge with short voltage pulses was to further increase discharge stability during the deposition by minimizing the number of microarcs on the V-W target and to utilize a different energetics of the reactive deposition process (particularly at the higher deposition-averaged target power density used, resulting in a high deposition rate of the W-doped VO_2 layers) compared with that during a standard HiPIMS deposition with separated high-power pulses at a much lower duty cycle.

In this paper, we report the discharge characteristics, and the population of chosen atomic neutral (V, O and Ar) and ionic (V^+, V^{2+}, O^+ and Ar^+) species in front of the sputter V-W target and of the substrate during low-temperature ($T_s = 350$ °C) depositions of W-doped VO_x films. The depositions were performed using reactive DOMS with a feedback pulsed O_2 flow control at various oxygen partial pressures, and at a constant target power and voltage pulse duration. The oxygen partial pressure, p_{O_2}, is an important process parameter significantly affecting not only the complicated physical and chemical processes on the sputter target and in the discharge plasma, which determine the time evolution of the target current and power during discharge pulses [17, 27], but also the processes on the surface of growing films [28].

The main aim of this work is to explain the interplay between the p_{O_2} oscillating around pre-selected critical values and the discharge characteristics, and the elemental composition, structure and thermochromic properties of the W-doped VO_x films produced. This is important for a further improvement of this new scalable sputter deposition technique for a fast low-temperature synthesis of high-performance durable thermochromic VO_2-based multilayer coatings for smart-window applications.

2. Experimental details

2.1. Film preparation

The W-doped VO_x films were deposited onto a 170 nm thick YSZ layer [24] on a 1 mm thick SLG substrate, and onto a Si(100) substrate using a strongly unbalanced magnetron source with a directly water-cooled single V-W (1.14 at.% corresponding to 4.0 wt.%) target (99.95% V and W purity, diameter of 100 mm and thickness of 6 mm) in a standard stainless-steel vacuum chamber (diameter of 507 mm and length of 520 mm), which was evacuated by a diffusion pump ($2\ m^3s^{-1}$) backed up with a rotary pump ($30\ m^3h^{-1}$). The base pressure before deposition was 10^{-3} Pa. A detailed characterization of the magnetic field and the degree of its unbalance is given in [29]. The substrates at the distance of 100 mm from the target were at a floating potential. The substrate surface temperature, maintained during the deposition by a built-in heating system, was 350 °C.

The magnetron was driven by a DOMS power supply (HIPIMS Cyprium plasma generator, Zpulser Inc.). In this work, the macropulse (composed of 10 micropulses) duration was 500 μs at a repetition frequency of 640 Hz. The micropulse on-time was 26 μs at a repetition frequency of 20 kHz within a macropulse (see figure 1). The deposition-averaged target power density (spatially averaged over the total target area), $\langle S_d \rangle$, was 34 W cm^{-2}.

Waveforms of the magnetron voltage, $U_d(t)$, and the discharge current, $I_d(t)$, were monitored (figure 1) and the $\langle S_d \rangle$ value was evaluated using the formula

$$\langle S_d \rangle = \frac{1}{t_e - t_s} \int_{t_s}^{t_e} U_d(t) J_t(t)\, dt. \quad (1)$$

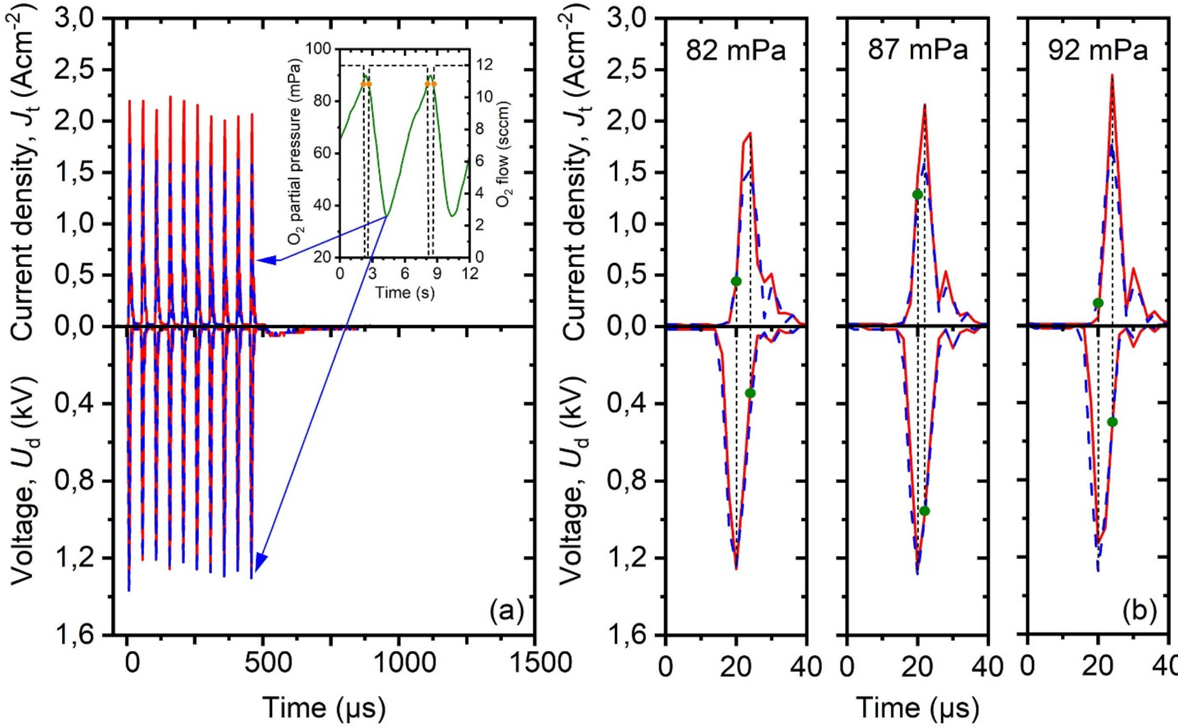

Figure 1. Waveforms of the magnetron voltage, U_d, and the target current density, J_t, for a 500 μs macropulse composed of 10 micropulses during a deposition of the strongly thermochromic W-doped VO_2 films (table 2) at a pre-selected critical value of the oxygen partial pressure $(p_{O_2})_{cr} = 87$ mPa (panel (a)). Time evolution of the oxygen partial pressure, p_{O_2}, during the deposition is shown in the inset of panel (a). The pre-selected critical value $(p_{O_2})_{cr} = 87$ mPa determining the switching-on and switching-off of the oxygen flow rate $\Phi_{O_2} = 12$ sccm is marked by dots. Typical waveforms for a micropulse with the same pulse-on time $t_{on} = 26$ μs at $(p_{O_2})_{cr} = 82$ mPa, 87 mPa and 92 mPa are shown in panel (b). In the main panels, the dashed (blue) and full (red) lines represent the waveforms (both U_d and J_t) measured at the minimum (indicated in panel (a)) and maximum p_{O_2}, during the deposition, respectively. The J_t values corresponding to the maximum $|U_d|$ and the U_d values corresponding to the maximum J_t during the micropulses are marked by dots in panel (b).

Here, the target current density $J_t(t) = I_d(t)/A_t$ where A_t is the total area of the target (78.54 cm^2 in our case), and t_s and t_e are the start and end times of the deposition. An analogous integral expression was used to calculate the deposition-averaged oxygen partial pressure, $\langle p_{O_2} \rangle$, from the monitored dependences of $p_{O_2}(t)$.

Oxygen was admitted into the vacuum chamber via mass flow controller and two corundum conduits. Two O_2 inlets with a diameter of 1 mm were placed symmetrically above the V-W target racetrack at the same distance of 20 mm from the V-W target surface and oriented to the substrate. The to-substrate O_2 injection into the dense plasma in front of the sputtered target is very suitable for reactive HiPIMS depositions of oxide films [28]. It leads to a substantially (2–3 times, as measured in [28]) increased local oxygen partial pressure in front of the O_2 inlets, compared with the p_{O_2} measured at the chamber wall, and to an enhanced flux of O atoms onto the substrate due to effective dissociation of the injected O_2 molecules [30] in the high-density plasma. As a consequence, the p_{O_2} needed for preparation of stoichiometric VO_2 films can be very low, resulting in the required low compound (oxide) fraction in the target surface layer. This is important for process stability, for increased sputtering of V and W atoms, and for low production of high-energy O^- ions.

The argon flow rate was 25 sccm corresponding to $p_{Ar} = 0.5$ Pa, while the total oxygen flow rate, Φ_{O_2}, in both conduits was alternating between 0 and 12 sccm (see figure 1). The moments of switching off the Φ_{O_2} pulses were determined during the deposition by a programmable logic controller using a pre-selected critical value of the oxygen partial pressure $(p_{O_2})_{cr} = 82$ mPa, 87 mPa (see the inset in figure 1(a)) and 92 mPa: when $p_{O_2}(t) < (p_{O_2})_{cr}$, $\Phi_{O_2} = 12$ sccm and when $p_{O_2}(t) \geqslant (p_{O_2})_{cr}$, $\Phi_{O_2} = 0$ sccm. The values of p_{Ar} and of $p_{Ar} + p_{O_2}$ were measured at the chamber wall using a high stability capacitance manometer (Baratron, Type 127, MKS) with the accuracy much better than 1%.

This feedback process control (see more details in [31]) makes it possible to deliver a high power into discharge pulses with minimized arcing on the target surface and thus, to utilize the exclusive benefits of the HiPIMS discharges (such as highly ionized fluxes of particles with high fractions of ionized sputtered V atoms onto the substrate and with enhanced energies and momenta of the ions bombarding the growing films [17], and a significantly increased chemisorption flux of O atoms and O^+ ions onto the substrate due to the used to-substrate O_2 injection into the dense plasma [28]) in the preparation of W-doped VO_2 films with a highly crystalline thermochromic VO_2 phase on unbiased substrates at low T_s.

Table 1. Characteristic data of the selected optical emission lines [33]. Here, λ is the line wavelength in air, E_m and g_m are the excitation energy and the statistical weight of the upper level m, respectively, and A_{mn} is the transition probability between the upper level m and the lower level n corresponding to the emission line.

Particle	λ (nm)	E_m (eV)	g_m	A_{mn} ($\times 10^7$ s^{-1})
Ar	751.47	13.27	1	4.0
Ar^+	448.18	21.50	6	4.55
O	777.42	10.74	5	3.69
O^+	298.04	32.98	8	0.149
V	372.90	5.18	8	2.01
V^+	319.07	5.01	9	12.5
V^{2+}	259.51	10.95	8	28.0

Here, it should be noted that the standard O_2 inlet at the wall of the vacuum chamber, when the flux of oxygen atoms and molecules onto the substrate is lower at the same p_{O_2} and the dissociation probability of O_2 molecules in the flux onto the substrate is much lower, resulted in a deposition of understoichiometric VO_x films. To deposit stoichiometric VO_2 films, the value of p_{O_2} had to be increased. However, this led to an increased compound (oxide) fraction in the target surface layer, resulting in a frequent arcing on the target surface and a lower deposition rate of films (see the analysis for ZrO_2 films in [32]).

2.2. Optical emission spectroscopy (OES)

Time-averaged OES was carried out using a grating spectrometer (Acton SP-2750i, Princeton Instruments, focal length of 750 mm, 1800 gr mm^{-1}) equipped with an ICCD camera (PI MAX 4, Princeton Instruments, 1024 $\times$ 256 imaging array, RB Fast Gate Intensifier) and a wavelength sorting filter wheel at the input. The light was collected by a rectangular (10 $\times$ 15 mm) collimator (length of 450 mm), positioned perpendicularly to the discharge axis and located at two distances from the target; namely, at $z = 10$ mm (in front of the target) and at $z = 90$ mm (in front of the substrate). A UV-VIS-NIR optical fiber interconnected the collimator and the spectrometer (see a similar OES system in [30]). The system sensitivity for different wavelengths in the range from 220 nm to 850 nm and the amplification of the light intensifier were calibrated using a deuterium and halogen light source, and a Na lamp, respectively. The measured values were averaged over 14 016 macropulse periods in 21.9 s for $z = 10$ mm and over 17 984 macropulse periods in 28.1 s for $z = 90$ mm.

The list of the monitored optical emission lines is given in table 1. The lines were chosen from the measured optical emission spectra in order to avoid overlapping with other emission lines. Note that no W and W^+ lines could be reliably identified mainly owing to a very low amount of the sputtered W atoms, compared to the V atoms, in the discharge (see only 1.14 at.% of W in the V-W target). No O_2 and O_2^+ emission lines were detected.

The density of the excited state $n_m(X)$ for a selected particle X was calculated (in arbitrary units) using $n_m(X) = N_{mn}(X)/A_{mn}$, where $N_{mn}(X)$ is the photon count per second and A_{mn} is the transition probability relating to the corresponding emission line [30]. The excitation temperature, T_{ex}, was determined from a slope of the Boltzmann plot constructed using the n_m values for 59 excited states of V^+ ions with $E_m \leqslant 7.1$ eV. These E_m values are sufficiently low to avoid the effect of a charge transfer between the Ar^+ ions and V atoms in ground states, which produces excited V^+ ions with $E_m \cong 9.01$ eV (given by the difference between the ionization energy of 15.76 eV for Ar atom and 6.75 eV for V atom [33]). Here, it should be mentioned that the T_{ex} follows trends of the electron temperature, T_e, particularly in a high-density plasma, but their values can be different [30, 34].

2.3. Film characterization

The elemental composition of the W-doped VO_x films was measured on dedicated 700–800 nm thick layers on Si (100) substrate in a scanning electron microscope (SU-70, Hitachi) using wave-dispersive spectroscopy (Magnaray, Thermo Scientific) at a low primary electron energy of 7.5 keV. Standard reference samples of pure V, W and Fe_2O_3 (Astimex Scientific Ltd) were utilized. Based on the standards´ purity and our experience, the measurement errors are estimated to be 0.04 at.% for W, 1 at.% for V and 2 at.% for O.

The room-temperature (25 °C) crystal structure of both W-doped VO_x and YSZ was characterized by x-ray diffraction (XRD) using a PANalytical X´Pert PRO diffractometer working with a CuKα (40 kV, 40 mA) radiation at a glancing incidence of 1°. The average size of coherently diffracting regions of the VO_2 (M1)/VO_2 (R) phase was estimated from the corrected full width at half maximum of the main VO_2 (M1)/VO_2 (R) diffraction peak using the Scherrer equation. At first, the diffraction peak was approximated by pseudo-Voigt function. Then, the calculated value of the full width at half maximum was corrected for instrumental broadening using a LaB_6 powder standard.

The thickness of individual layers was measured by spectroscopic ellipsometry using the J. A. Woollam Co. Inc. VASE instrument [24].

The normal-incidence transmittance, T, of the coatings (W-doped VO_x films on YSZ layer) was measured by spectrophotometry using the Agilent CARY 7000 instrument equipped with an in-house made heating/cooling cell. Spectroscopic measurements were performed in the wavelength range $\lambda = 300$ nm–2500 nm at the temperatures $T_{ms} = -20$ °C (semiconducting state below T_{tr}) and $T_{mm} = 70$ °C (metallic state above T_{tr}). Hysteresis curves were measured at $\lambda = 2500$ nm in the temperature range $T_m = -20$ °C to 70 °C. The coating performance is quantified by means of integral luminous transmittance, T_{lum}, and modulation of the solar energy transmittance, ΔT_{sol}, which are defined as

$$T_{lum}(T_m) = \frac{\int_{380}^{780} \varphi_{lum}(\lambda)\,\varphi_{sol}(\lambda)\,T(T_m,\lambda)\,d\lambda}{\int_{380}^{780} \varphi_{lum}(\lambda)\,\varphi_{sol}(\lambda)\,d\lambda} \quad (2)$$

and

$$\Delta T_{sol} = T_{sol}(T_{ms}) - T_{sol}(T_{mm}), \quad (3)$$

where

$$T_{\mathrm{sol}}\left(T_{\mathrm{m}}\right)=\frac{\int_{300}^{2500}\varphi_{\mathrm{sol}}\left(\lambda\right)T\left(T_{\mathrm{m}},\lambda\right)\mathrm{d}\lambda}{\int_{300}^{2500}\varphi_{\mathrm{sol}}\left(\lambda\right)\mathrm{d}\lambda}. \quad (4)$$

Here, φ_{lum} is the luminous sensitivity of the human eye and φ_{sol} is the sea-level solar irradiance spectrum at an air mass of 1.5 [35].

3. Results and discussion

3.1. Discharge characteristics

Figure 1 shows the time evolution of the magnetron voltage, $U_{\mathrm{d}}(t)$, and the target current density, $J_{\mathrm{t}}(t)$, which are related to the minimum and maximum values of $p_{\mathrm{O_2}}$ during depositions of the W-doped VO_x films at a fixed deposition- averaged target power density of 34 W $\mathrm{cm^{-2}}$ and various critical values of the oxygen partial pressure $(p_{\mathrm{O_2}})_{\mathrm{cr}}$ = 82 mPa, 87 mPa and 92 mPa. Thus, figure 1 shows the ranges of the waveforms of $U_{\mathrm{d}}(t)$ and $J_{\mathrm{t}}(t)$ during the controlled depositions with $p_{\mathrm{O_2}}$ oscillating between 27 mPa and 90 mPa at the deposition-averaged value $\langle p_{\mathrm{O_2}}\rangle$ = 59 mPa, between 33 mPa and 92 mPa at $\langle p_{\mathrm{O_2}}\rangle$ = 63 mPa, and between 35 mPa and 98 mPa at $\langle p_{\mathrm{O_2}}\rangle$ = 67 mPa (table 2).

As seen in figure 1(b), an increase in $(p_{\mathrm{O_2}})_{\mathrm{cr}}$ results in higher maximum J_{t} values during the J_{t} micropulses with narrower peaks at slightly decreasing maximum $|U_{\mathrm{d}}|$ values. The higher J_{t} at the higher $p_{\mathrm{O_2}}$, leading to a larger target coverage by an oxide, can be explained by three effects: (1) A higher density of O_2 molecules and O atoms (arising in front of the target by an O_2 dissociation and by an intense sputtering from the target [28]) results in a significantly enlarged flux of the O_2^+ and O^+ ions onto the target. For the highest $(p_{\mathrm{O_2}})_{\mathrm{cr}}$ = 92 mPa, a to-target flux of the O^+ ions produced close to the target from the O atoms preferentially sputtered from the target surface becomes particularly important [27]. (2) The O^+ and O_2^+ induced secondary-electron emission coefficients of the target surface may be higher than that induced by Ar^+ ions [27, 36]. (3) The secondary-electron emission coefficient of the partly oxidized V-W target may increase with the target coverage by an oxide [37].

The quick increase of $J_{\mathrm{t}}(t)$ with the rising $|U_{\mathrm{d}}(t)|$ during a micropulse for $(p_{\mathrm{O_2}})_{\mathrm{cr}}$ = 87 mPa resulted in an only small delay (2 μs) of the maximum J_{t} compared to the maximum $|U_{\mathrm{d}}|$. As a consequence, the maximum target power density in a micropulse, $(S_{\mathrm{d}})_{\mathrm{max}}$, oscillated between the highest values of 2.11 $\mathrm{kWcm^{-2}}$ and 2.62 $\mathrm{kWcm^{-2}}$ (table 2), and a high energy corresponding to the target power density $S_{\mathrm{d}} \geqslant 1.5$ $\mathrm{kWcm^{-2}}$ was delivered into the discharge at a relatively high $|U_{\mathrm{d}}| \geqslant 1.0$ kV and $J_{\mathrm{t}} \geqslant 1.5$ $\mathrm{Acm^{-2}}$ for almost 1 μs (minimum $p_{\mathrm{O_2}}$) and 2 μs (maximum $p_{\mathrm{O_2}}$) during each micropulse under these conditions (see figure 1). In the case of $(p_{\mathrm{O_2}})_{\mathrm{cr}}$ = 82 mPa and 92 mPa, the aforementioned delay between the maximum J_{t} and $|U_{\mathrm{d}}|$ was approximately 4 μs, the $(S_{\mathrm{d}})_{\mathrm{max}}$ oscillated between much lower values of 1.32 $\mathrm{kWcm^{-2}}$ and 1.46 $\mathrm{kWcm^{-2}}$, and of 1.45 $\mathrm{kWcm^{-2}}$ and 1.51 $\mathrm{kWcm^{-2}}$, respectively (table 2), and the sputtering of the V-W target with $|U_{\mathrm{d}}| \geqslant 1.0$ kV could be performed only at much lower target power densities than 1.5 $\mathrm{kWcm^{-2}}$.

In standard reactive HiPIMS discharges, an initial increase in the discharge current is slower for a higher $p_{\mathrm{O_2}}$ during a deposition, particularly at a larger target coverage by an oxide [17, 27]. In DOMS discharges, however, the initial onset of the discharge current is accelerated by a high electron density, n_{e}, at the beginning of magnetron voltage micropulses with a very short micropulse off-time (24 μs in this work). Taking into account the correlation between the higher $(S_{\mathrm{d}})_{\mathrm{max}}$ and the broadening of the energy distributions of ionized sputtered atoms at a substrate position during HiPIMS depositions [38, 39], the investigated DOMS regime with $(p_{\mathrm{O_2}})_{\mathrm{cr}}$ = 87 mPa is the most appropriate for production of highly ionized fluxes of particles with high fractions of ionized sputtered V atoms, which bombard the growing films with enhanced energies (see the improved crystallinity of the W-doped VO_2 films discussed later). Recall that the high-energy parts of the energy distributions for the V^+, V^{2+} and O^+ ions [17] originate from the Thompson energy distribution of sputtered V and O atoms, respectively, which is superimposed with energy gains caused by localized potential humps formed in ionization zones (plasma spokes) close to the target [39, 40]. The effect of the spoke regions on the ionization of Ar atoms and O_2 molecules is much weaker as their densities near the target are significantly reduced [30] mainly due to a momentum transfer from the sputtered V atoms during high-power pulses. In the case of the O^+ ions, a backscattering (reflection) of light O atoms from the sputtered V-W target partly covered by a V (or W) oxide can be also important [17].

3.2. Population of chosen atomic and ionic species in the discharge

Figure 2(a) shows the time-averaged densities of the excited states, $n_{\mathrm{m}}(X)$, for the considered particles in front of the target (z = 10 mm) and of the substrate (z = 90 mm). The $n_{\mathrm{m}}(X)$ values are related to the corresponding ground-state densities $n_1(X)$ and to the excitation and ionization processes at a given discharge position during a macropulse. In a general case, the local excitation and ionization processes are strongly dependent on n_{e} and T_{e} (see, for example [41, 42], and the works cited therein). As can be seen in figure 2(b), the T_{ex} values are almost the same for both positions in the discharge at $(p_{\mathrm{O_2}})_{\mathrm{cr}}$ = 87 mPa. No changes in these T_{ex} were observed for both positions at 82 mPa and 92 mPa (not presented graphically).

Taking into account the aforementioned correlation between T_{ex} and T_e, we can state that a large decrease of the densities $n_{\mathrm{m}}(X)$ for z = 90 mm, which was observed for all particles excepting the Ar and O atoms, is caused predominantly by a significant weakening of the excitation and ionization processes owing to a reduced local values of n_{e}. In addition, a radial expansion of the volume occupied by plasma and sputtered particles with a growing distance from the target resulted in a local decrease of the ground-state densities n_1(X). The main reason for a small decrease of the n_{m}(Ar) for z = 90 mm is a much higher n_1(Ar) than that for z = 10 mm.

Table 2. Deposition characteristics, elemental compositions of the W-doped VO_x films and their thermochromic properties at the same deposition-averaged target power density of 34 Wcm^{-2} and the pre-selected critical values of the oxygen partial pressure $(p_{O_2})_{cr}$ = 82 mPa, 87 mPa and 92 mPa (see figure 1). Here, $\langle p_{O_2}\rangle$ is the deposition-averaged oxygen partial pressure, $(S_d)_{max}$ is the maximum target power density in a micropulse, a_D is the deposition rate of the films, T_{lum} and ΔT_{sol} is the integral luminous transmittance and the modulation of the solar energy transmittance of the W-doped VO_x films on YSZ layer, respectively, and T_{tr} is their transition temperature.

Deposition characteristics					Composition of films			Thermochromic properties		
$(p_{O_2})_{cr}$ (mPa)	p_{O_2} (mPa)	$\langle p_{O_2}\rangle$ (mPa)	$(S_d)_{max}$ (kW cm^{-2})	a_D (nm min^{-1})	V	W (at.%)	O	T_{lum} (%)	ΔT_{sol} (%)	T_{tr} (°C)
82	27–90	59	1.32–1.46	56	36.2	0.42	63.4	29.8	1.5	—
87	33–92	63	2.11–2.62	53	34.5	0.48	65.0	40.9	8.9	28
92	35–98	67	1.45–1.51	41	32.5	0.47	67.0	58.6	0.7	—

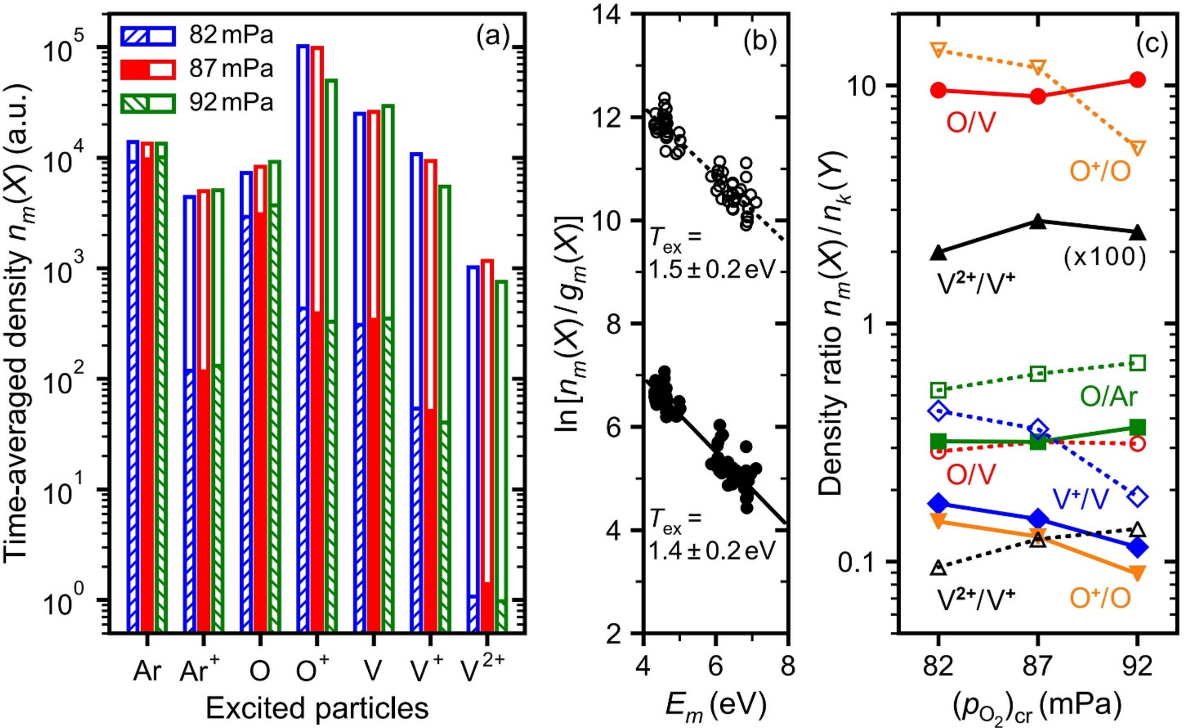

Figure 2. Time-averaged densities of the excited states, $n_m(X)$, for the considered atoms and ions in front of the sputter target for z = 10 mm (empty columns) and of the substrate for z = 90 mm (full and hatched columns) at various critical values of the oxygen partial pressure $(p_{O_2})_{cr}$ = 82 mPa, 87 mPa and 92 mPa (panel (a)). The excitation temperatures, T_{ex}, determined from the slopes of the Boltzmann plots constructed from the densities of the V^+ excited states measured for z = 10 mm (empty symbols) and z = 90 mm (full symbols) at $(p_{O_2})_{cr}$ = 87 mPa (panel (b)). Density ratios for the excited states, $n_m(X)/n_k(Y)$, of the considered atoms and ions for z = 10 mm (dashed lines) and z = 90 mm (full lines) at $(p_{O_2})_{cr}$ = 82 mPa, 87 mPa and 92 mPa (panel (c)).

In front of the substrate, the n_1(Ar) is much less reduced by a weaker electron-impact ionization (the ionization energy of 15.76 eV) and by a much weaker 'sputtering wind' than in front of the sputter target. The main reason for a relatively small difference in the n_m(O) for z = 10 mm and 90 mm is the to-substrate O_2 injection into a dense plasma in front of the target (at z = 20 mm). A substantially increased local oxygen partial pressure in front of the O_2 inlets and an effective electron-impact dissociation of O_2 molecules in the high-density plasma [30] resulted in a large flux of O atoms onto the substrate. In addition, the n_1(O) was much less reduced by a weaker electron-impact ionization (the ionization energy of 13.62 eV) than in front of the sputter target. Here, it should be mentioned that an enlarged fraction of oxygen atomic (O and O^+) species, compared with oxygen molecular (O_2 and O_2^+) species, in the chemisorption flux of oxygen particles onto the substrate is of key importance for reactive sputter deposition of oxide films, as the sticking coefficients of the oxygen atomic species on the non-oxidized (metal) part of the substrate surface are much higher than those of the oxygen molecular species (see [28] and the works cited therein).

The density ratios $n_m(X)/n_k(Y)$ in figure 2(c) provide important qualitative information on the corresponding ground-state density ratios $n_1(X)/n_1(Y)$ in front of the target and the substrate. Thereby, they contribute to the explanation of the processes during the deposition of the W-doped VO_x films at the $(p_{O_2})_{cr}$ in the range from 82 mPa to 92 mPa, when the V content in the films decreased from 36.2 ± 1.0 at.% to 32.5 ± 1.0 at.% (see table 2), while the O content in the films increased from 63.4 ± 2.0 at.% to 67.0 ± 2.0 at.%,

respectively. A higher $\langle p_{O_2}\rangle$ in the vacuum chamber resulted in an expected lowering of the deposition rate of the films, a_D, owing to a larger coverage of the V-W target by an oxide [28]. The high $n_m(O)/n_k(V)$ and the relatively high $n_m(O)/n_k(Ar)$ in front of the substrate ($z = 90$ mm; see figure 2(c)) are a consequence of the used to-substrate configuration of the O_2 inlets with their optimized position in the discharge. Let us quantify that both these ratios $n_m(O)/n_k(V)$ and $n_m(O)/n_k(Ar)$ in front of the substrate increase 1.2 times when $(p_{O_2})_{cr}$ increases from 87 to 92 mPa, and let us emphasize the significance of this increase. The factor 1.2 is, for example, even higher than that which represents the difference between the phases identified by XRD in the next section, VO_2 and V_4O_9 (the [O]/[V] ratio in the latter is 1.125 × higher). The high $n_m(O^+)/n_k(O)$ for $z = 10$ mm is a result of the electron-impact ionization of the O atoms diffusing to the target and being sputtered from the target. A decrease of the $n_m(O^+)/n_k(O)$ at the highest $(p_{O_2})_{cr} = 92$ mPa, when the target surface is more oxidized (see the reduced $a_D = 41$ nm min^{-1} in table 2), is predominantly caused by a higher to-target flux of the O^+ ions produced close to the target ($z < 10$ mm) from the O atoms preferentially sputtered from the target surface [27]. The values of the $n_m(V^+)/n_k(V)$ measured for $z = 10$ mm are relatively high, although they are reduced by the electron-impact ionization of the V^+ ions, producing V^{2+} ions (see figure 2(c)), and by a to-target flux of the V^+ ions arising close to the target ($z < 10$ mm) from the V atoms sputtered mainly from a non-oxidized part of the target which is smaller at a higher $(p_{O_2})_{cr}$ [28]. Using the relations $\Gamma_i \propto T_e^{1/2}$ and $\Gamma_a \propto T_a^{1/2}$, where T_a is the atom thermal temperature, for the fluxes of ions, Γ_i, and neutral atoms, Γ_a, onto the substrate [43] and taking into account that T_e is much higher than T_a in our case (see figure 2(b)), we can state that the growing films are bombarded by high fluxes of the V^+ and O^+ ions, particularly for $(p_{O_2})_{cr} = 82$ mPa and 87 mPa.

3.3. *Film structure and properties*

The phase structure of the W-doped VO_x films is shown in figure 3. The crystalline phases taken into account include YSZ (PDF [44] #04-021-9607), VO_2(M1) (#04-003-2035), VO_2(R) (#01-073-2362), VO_2(B) (#04-007-0514) and V_4O_9 (also referred to as $(VO)_2(V_2O_7)$ in PDF; #04-017-0339). Let us emphasize that there is no need to distinguish between VO_2(M1) and VO_2(R): these two sets of very similarly positioned peaks represent the same thermochromic material (at a transition temperature close to the measurement temperature, see figure 4). First, the figure confirms the crystallinity of the YSZ antireflection template [24]: see the same set of YSZ peaks in all XRD patterns including that taken from the uncoated template. Second and most importantly, the evolution of peaks arising from W-doped VO_x prepared at $(p_{O_2})_{cr}$ increasing from 82 mPa to 92 mPa represents a superposition of two effects discussed in the previous section and summarized in table 2: monotonically increasing O content, and non-monotonically changing $(S_d)_{max}$. The former effect is best visible from the transition from $(p_{O_2})_{cr} = 87$ mPa to $(p_{O_2})_{cr} = 92$ mPa: the slight enhancement of the O

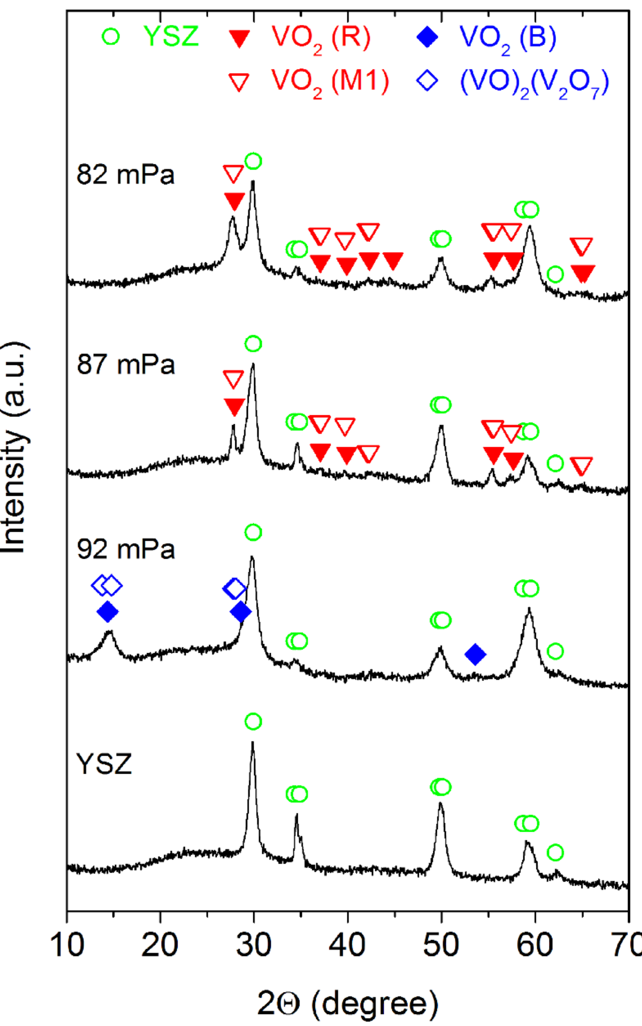

Figure 3. X-ray diffraction patterns taken at $T_m = 25$ °C from the W-doped VO_x films with the thickness of 71 nm, 67 nm and 52 nm deposited at various critical values of the oxygen partial pressure $(p_{O_2})_{cr} = 82$ mPa, 87 mPa and 92 mPa, respectively, onto a 170 nm thick YSZ layer on a 1 mm thick glass substrate. For comparison, the x-ray diffraction pattern from the corresponding 170 nm thick YSZ layer on the same substrate is given. The main diffraction peaks of VO_2 (M1), VO_2 (R), VO_2 (B), $(VO)_2(V_2O_7)$ and YSZ (tetragonal $Y_{0.06}Z_{0.94}O_{1.97}$) are marked.

content is sufficient for a replacement of thermochromic VO_2(M1)/VO_2(R) by non-thermochromic V_4O_9 with a possible slight contribution of VO_2(B) (let alone an amorphous phase). The latter effect is best visible from the transition from $(p_{O_2})_{cr} = 82$ mPa to $(p_{O_2})_{cr} = 87$ mPa: the only crystalline phase exhibited by both films is VO_2(M1)/VO_2(R), but at a very different crystal size estimated from the width of the peak around $2\theta = 28°$ (VO_2(M1) (011)/VO_2(R) (110)). While the relatively low energy and momentum delivered to growing films at $(p_{O_2})_{cr} = 82$ mPa and the resulting $(S_d)_{max} = 1.32$–1.46 kWcm^{-2} lead to only 11 nm large coherently diffracting regions, the high energy and momentum delivered to growing films by bombarding particles (including many V^+ ions) at $(p_{O_2})_{cr} = 87$ mPa and the resulting $(S_d)_{max} = 2.11$–2.62 kWcm^{-2} lead to 36 nm large coherently

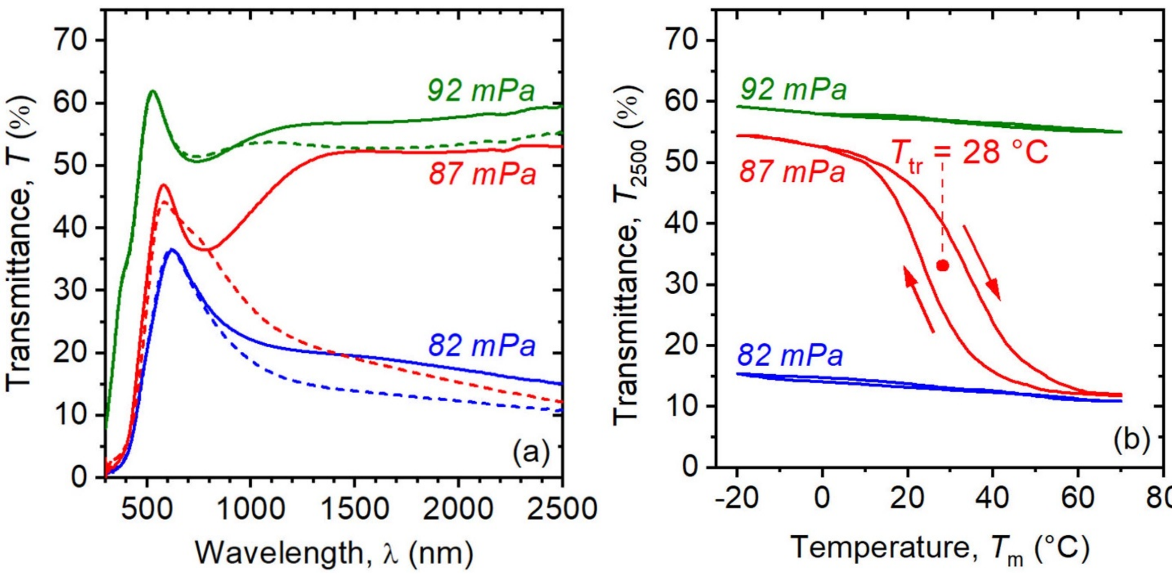

Figure 4. Spectral transmittance (a) at $T_{ms} = -20$ °C (full lines) and $T_{mm} = 70$ °C (dashed lines), and temperature dependence of the transmittance at 2500 nm (b) for the W-doped VO_x films with the thickness of 71 nm, 67 nm and 52 nm deposited at various critical values of the oxygen partial pressure $(p_{O_2})_{cr} = 82$ mPa, 87 mPa and 92 mPa, respectively, onto a 170 nm thick YSZ layer on a 1 mm thick glass substrate. The transition temperature, T_{tr}, is given in panel (b).

diffracting regions. This has a major impact on the strength of the thermochromic transition.

The thermochromic properties of the films are shown in figure 4. Figure 4(a) clearly shows that first, too low $(p_{O_2})_{cr} = 82$ mPa leads only to a weak thermochromic transition due to a combination of too low O content and too low size of those VO_2(M1)/VO_2(R) crystals which nevertheless formed (previous paragraph). Thus, there is a low $T(\lambda)$ in the infrared in the whole T_m range. Second, the optimum $(p_{O_2})_{cr} = 87$ mPa leads to a strong thermochromic transition due to a combination of almost optimum O content and exceptionally energetic bombardment which guarantees the formation of large VO_2(M1)/VO_2(R) crystals. Third, too high $(p_{O_2})_{cr} = 92$ mPa once again leads only to a weak thermochromic transition, this time due to too high O content leading to a dominance of other phases than VO_2(M1)/VO_2(R). Thus, there is a high $T(\lambda)$ in the infrared in the whole T_m range. Furthermore, the figure confirms that $T(\lambda)$ in the visible is (1) almost temperature-independent (indeed, most of the energy saving takes place in the infrared) and (2) increasing with increasing $(p_{O_2})_{cr}$ from 82 mPa through 87 mPa to 92 mPa. The latter is not only due to the increasing O content, but also due to decreasing deposition rate from 56 nm min^{-1} through 53 nm min^{-1} to 41 nm min^{-1} (film thickness of 71 nm, 67 nm and 52 nm, respectively). In other words, the [O]/[V + W] ratio in the films does not increase because of increasing rate of O incorporation, but because the rate of metal incorporation decreases even faster than the rate of O incorporation. Let us recall the discussion in sections 3.1 and 3.2, at the first place the partial target oxidation supported by the to-target flux of the O^+ ions.

The quantified coating performance in terms of T_{lum} and ΔT_{sol} (table 2) is of limited importance in the present paper focused on the deposition process, because the coatings do not include the state-of-the-art second order antireflection overlayer [45] used in our papers focused on the coating performance [24]. However, even the present values $T_{lum} = 40.9\%$ and $\Delta T_{sol} = 8.9\%$ achieved at the optimum $(p_{O_2})_{cr} = 87$ mPa without any antireflection overlayer (should lead to $T_{lum} \approx 49\%$ and $\Delta T_{sol} \approx 13\%$ with an antireflection overlayer) exhibit a clear superiority over $\Delta T_{sol} \leqslant 1.5\%$ achieved at suboptimum $(p_{O_2})_{cr} = 82$ mPa and 92 mPa. Furthermore, the performance of the coating prepared at $(p_{O_2})_{cr} = 87$ mPa is complemented by the low thermochromic transition temperature $T_{tr} = 28$ °C, demonstrating the ability of the presented preparation technique (contrary to some other techniques—in [8]) to dope VO_2 by W without suppressing the thermochromic effect.

4. Conclusions

The discharge characteristics, and population of chosen atomic neutral (V, O and Ar) and ionic (V^+, V^{2+}, O^+ and Ar^+) species in the discharge were investigated during controlled low-temperature (350 °C) reactive DOMS depositions of W-doped VO_x films without a substrate bias voltage. It was found that setting of the amount of O_2 in the gas mixture determines not only the elemental and phase composition of the films and their deposition rate but also the crystallinity (by means of increased ion energies and momenta) of the thermochromic VO_2 phase in them. The OES measurements, performed in front of the V-W target and the substrate, contributed to the explanation of the processes during the depositions of the W-doped VO_x films at different $(p_{O_2})_{cr}$. These measurements confirmed a relatively high density of O atoms in front of the substrate, which

is a consequence of the used to-substrate O_2 injection into a dense plasma in front of the sputter target. The crystalline W-doped VO_2 films with a low transition temperature $T_{tr} = 28\,^{\circ}C$ exhibited a high modulation of the solar energy transmittance $\Delta T_{sol} = 8.9\%$.

We have thus demonstrated a great potential of the controlled reactive DOMS for a fast (53 nm min^{-1} in this work) low-temperature preparation of large-area thermochromic VO_2-based coatings for future energy-saving smart windows.

Data availability statement

All data that support the findings of this study are included within the article (and any supplementary files).

Acknowledgments

This work was supported by the Czech Science Foundation under Project No. 21-28277S.

ORCID iDs

Jaroslav Vlček https://orcid.org/0000-0003-2627-2074
Michal Kaufman https://orcid.org/0009-0001-1733-2998
Andrea Dagmar Pajdarová https://orcid.org/0000-0002-0836-5624
Jiří Houška https://orcid.org/0000-0002-4809-4128

References

[1] Morin F J 1959 Oxides which show a metal-to-insulator transition at the Neel temperature *Phys. Rev. Lett.* **3** 34–36
[2] Liu K, Lee S, Yang S, Delaire O and Wu J 2018 Recent progresses on physics and applications of vanadium dioxide *Mater. Today* **21** 875
[3] Ke Y, Wang S, Liu G, Li M, White T J and Long Y 2018 Vanadium dioxide: the multistimuli responsive material and its applications *Small* **14** 1802025
[4] Shi R, Shen N, Wang J, Wang W, Amini A, Wang N and Cheng C 2019 Recent advances in fabrication strategies, phase transition modulation, and advanced applications of vanadium dioxide *Appl. Phys. Rev.* **6** 011312
[5] Cao X, Chang T, Shao Z, Xu F, Luo H and Jin P 2020 Challenges and opportunities toward real application of VO_2-based smart glazing *Matter* **2** 862–81
[6] Xue Y and Yin S 2022 Element doping: a marvelous strategy for pioneering the smart applications of VO_2 *Nanoscale* **14** 11054–97
[7] Haddad E, Kruzelecky R V, Murzionak P, Jamroz W, Tagziria K, Chaker M and Ledrogoff B 2022 Review of the VO_2 smart material applications with emphasis on its use for spacecraft thermal control *Front. Mater.* **9** 1013848
[8] Houska J 2022 Design and reactive magnetron sputtering of thermochromic coatings *J. Appl. Phys.* **131** 110901
[9] Sun G, Cao X, Li X, Bao S, Li N, Liang M, Gloter A, Gu H and Jin P 2017 Low-temperature deposition of VO_2 films with high crystalline degree by embedding multilayered structure *Sol. Energy Mater. Sol. Cells* **161** 70–76
[10] Chang T, Cao X, Li N, Long S, Gao X, Dedon L R, Sun G, Luo H and Jin P 2017 Facile and low-temperature fabrication of thermochromic Cr_2O_3/VO_2 smart coatings: enhanced solar modulation ability, high luminous transmittance and UV-shielding function *ACS Appl. Mater. Interfaces* **9** 26029–37
[11] Chang T-C, Cao X, Bao S-H, Ji S-D, Luo H-J and Jin P 2018 Review on thermochromic vanadium dioxide based smart coatings: from lab to commercial application *Adv. Manuf.* **6** 1–19
[12] Zhang Y, Li B, Wang Z, Tian S, Liu B, Zhao X, Li N, Sankar G and Wang S 2021 Facile preparation of $Zn_2V_2O_7$–VO_2 composite films with enhanced thermochromic properties for smart windows *ACS Appl. Electron. Mater.* **3** 2224–32
[13] Fahland M, Zywitzki O, Modes T, Vondkar K, Werner T, Ottermann C, Berendt M and Pollack G 2019 Roll-to-roll sputtering of indium tin oxide layers onto ultrathin flexible glass *Thin Solid Films* **669** 56–59
[14] Rezek J, Szelwicka J, Vlček J, Čerstvý R, Houška J, Fahland M and Fahlteich J 2022 Transfer of the sputter technique for deposition of strongly thermochromic VO_2-based coatings on ultrathin flexible glass to large-scale roll-to-roll device *Surf. Coat. Technol.* **442** 128273
[15] Fortier J-P, Baloukas B, Zabeida O, Klemberg-Sapieha J E and Martinu L 2014 Thermochromic VO_2 thin films deposited by HiPIMS *Sol. Energy Mater. Sol. Cells* **125** 291–6
[16] Aijaz A, Ji Y-X, Montero J, Niklasson G A, Granqvist C G and Kubart T 2016 Low-temperature synthesis of thermochromic vanadium dioxide thin films by reactive high power impulse magnetron sputtering *Sol. Energy Mater. Sol. Cells* **149** 137–44
[17] Vlček J, Kolenatý D, Kozák T, Houška J, Čapek J and Kos Š 2019 Ion-flux characteristics during low-temperature (300 °C) deposition of thermochromic VO_2 films using controlled reactive HiPIMS *J. Phys. D: Appl. Phys.* **52** 025205
[18] Miao L, Peng Y, Wang D, Liang J, Hu C, Nishibori E, Sun L, Fisher C A J and Tanemura S 2020 Characterisation of the temperature-dependent M_1 to R phase transition in W-doped VO_2 nanorod aggregates by Rietveld refinement and theoretical modelling *Phys. Chem. Chem. Phys.* **22** 7984–94
[19] Zhang J, He H, Xie Y and Pan B 2013 Theoretical study on the tungsten-induced reduction of transition temperature and the degradation of optical properties of VO_2 *J. Chem. Phys.* **138** 114705
[20] Loquai S, Baloukas B, Klemberg-Sapieha J E and Martinu L 2017 HiPIMS-deposited thermochromic VO_2 films with high environmental stability *Sol. Energy Mater. Sol. Cells* **160** 217–24
[21] Baloukas B, Loquai S and Martinu L 2018 VO_2-based thermally active low emissivity coatings *Sol. Energy Mater. Sol. Cells* **183** 25–33
[22] Victor J L, Marcel C, Sauques L, Penin N and Rougier A 2021 High quality thermochromic VO_2 thin films deposited at room temperature by balanced and unbalanced HiPIMS *Sol. Energy Mater. Sol. Cells* **227** 111113
[23] Kolenatý D, Vlček J, Bárta T, Rezek J, Houška J and Haviar S 2020 High-performance thermochromic VO_2-based coatings with a low transition temperature deposited on glass by a scalable technique *Sci. Rep.* **10** 11107
[24] Kaufman M, Vlček J, Houška J, Čerstvý R, Farrukh S, Chargaoui M, Haviar S, Jiang J C, Meletis E I and Kos Š 2023 High-performance thermochromic $YSZ/V_{0.986}W_{0.014}O_2/YSZ$ coatings for energy-saving smart windows *Sol. Energy Mater. Sol. Cells* submitted
[25] Ferreira F, Sousa C, Cavaleiro A, Anders A and Oliveira J 2017 Phase tailoring of tantalum thin films deposited in deep oscillation magnetron sputtering mode *Surf. Coat. Technol.* **314** 97–104
[26] Lin J 2019 High rate reactive sputtering of Al_2O_3 coatings by HiPIMS *Surf. Coat. Technol.* **357** 402–11
[27] Aiempanakit M, Aijaz A, Lundin D, Helmersson U and Kubart T 2013 Understanding the discharge current

behavior in reactive high power impulse magnetron sputtering of oxides *J. Appl. Phys.* **113** 133302
[28] Kozák T and Vlček J 2016 A parametric model for reactive high-power impulse magnetron sputtering of films *J. Phys. D: Appl. Phys.* **49** 055202
[29] Kudláček P, Vlček J, Burcalová K and Lukáš J 2008 Highly ionized fluxes of sputtered titanium atoms in high-power pulsed magnetron discharges *Plasma Sources Sci. Technol.* **17** 025010
[30] Pajdarová A D, Vlček J and Rezek J 2017 Optical emission spectroscopy during the deposition of zirconium dioxide films by controlled reactive high-power impulse magnetron sputtering *J. Appl. Phys.* **121** 171908
[31] Vlček J, Rezek J, Houška J, Čerstvý R and Bugyi R 2013 Process stabilization and a significant enhancement of the deposition rate in reactive high-power impulse magnetron sputtering of ZrO_2 and Ta_2O_5 films *Surf. Coat. Technol.* **236** 550–5
[32] Kozák T and Vlček J 2017 Dynamics of processes during the deposition of ZrO_2 films by controlled reactive high-power impulse magnetron sputtering: a modelling study *J. Appl. Phys.* **122** 043304
[33] Kramida A, Ralchenko Y and Reader J (NIST ASD Team) 2022 NIST atomic spectra database (version 5.10) (National Institute of Standards and Technology) (available at: https://physics.nist.gov/asd) (Accessed 26 March 2023)
[34] Chung T H, Kang H R and Bae M K 2012 Optical emission diagnostics with electric probe measurements of inductively coupled $Ar/O_2/Ar-O_2$ plasmas *Phys. Plasmas* **19** 113502
[35] (Available at: http://rredc.nrel.gov/solar/spectra/am1.5/; http://hyperphysics.phy-astr.gsu.edu/hbase/vision/efficacy.html) (Accessed 14 June 2016)
[36] Yamauchi Y and Shimizu R 1983 Secondary electron emission from aluminum by argon and oxygen ion bombardment below 3 keV *Jpn. J. Appl. Phys.* **22** L227
[37] Phelps A V and Petrovic Z L 1999 Cold-cathode discharges and breakdown in argon: surface and gas phase production of secondary electrons *Plasma Sources Sci. Technol.* **8** R21
[38] Aiempanakit M, Helmersson U, Aijaz A, Larsson P, Magnusson R, Jensen J and Kubart T 2011 Effect of peak power in reactive high power impulse magnetron sputtering of titanium dioxide *Surf. Coat. Technol.* **205** 4828–31
[39] Maszl C, Breilman W, Benedikt J and von Keudell A 2014 Origin of the energetic ions at the substrate generated during high power pulsed magnetron sputtering of titanium *J. Phys. D: Appl. Phys.* **47** 224002
[40] Panjan M, Franz R and Anders A 2014 Asymmetric particle fluxes from drifting ionization zones in sputtering magnetrons *Plasma Sources Sci. Technol.* **23** 025007
[41] Vlček J, Forejt L and van der Mullen J A M 1997 Magnesium as a representative analyte metal in argon inductively coupled plasmas. II. Population mechanisms in analytical zones of different spectrochemical systems *Spectrochim. Acta* B **52** 609–19
[42] Rudolph M, Revel A, Lundin D, Hajihoseini H, Brenning N, Raadu M A, Anders A, Minea T M and Gudmundsson J T 2021 On the electron energy distribution function in the high power impulse magnetron sputtering discharge *Plasma Sources Sci. Technol.* **30** 045011
[43] Kersten H 2001 *Modeling of Plasma-wall Interaction. In Low Temperature Plasma Physics, Fundamental Aspects and Applications* ed R Hippler, S Pfau, M Schmidt and K H Schoenbach (Wiley) pp 113–30
[44] The International Centre for Diffraction Data 2022 *PDF-4+ Database* (The International Centre for Diffraction Data)
[45] Houska J, Kolenaty D, Vlcek J, Barta T, Rezek J and Cerstvy R 2019 Significant improvement of the performance of $ZrO_2/V_{1-x}W_xO_2/ZrO_2$ thermochromic coatings by utilizing a second-order interference *Sol. Energy Mater. Sol. Cells* **191** 365–71